Published online 23 March 2022

Nucleic Acids Research, 2022, Vol. 50, No. 12 ***e69***
https://doi.org/10.1093/nar/gkac191

Optical control of protein delivery and partitioning in the nucleolus

Peng Tan[1,2,*], Tingting Hong[3], Xiaoli Cai[3], Wenbo Li[4], Yun Huang[3], Lian He[1,*] and Yubin Zhou[1,5,*]

[1]Center for Translational Cancer Research, Institute of Biosciences and Technology, Texas A&M University, Houston, TX 77030, USA, [2]Klarman Cell Observatory, Broad Institute of MIT and Harvard, Cambridge, MA 02142, USA, [3]Center for Epigenetics and Disease Prevention, Institute of Biosciences and Technology, Texas A&M University, Houston, TX 77030, USA, [4]Department of Biochemistry and Molecular Biology, McGovern Medical School, University of Texas Health Science Center, Houston, TX 77030, USA and [5]Department of Translational Medical Sciences, College of Medicine, Texas A&M University, Houston, TX 77030, USA

Received January 05, 2021; Revised February 12, 2022; Editorial Decision March 08, 2022; Accepted March 11, 2022

ABSTRACT

The nucleolus is a subnuclear membraneless compartment intimately involved in ribosomal RNA synthesis, ribosome biogenesis and stress response. Multiple optogenetic devices have been developed to manipulate nuclear protein import and export, but molecular tools tailored for remote control over selective targeting or partitioning of cargo proteins into subnuclear compartments capable of phase separation are still limited. Here, we report a set of single-component photoinducible nucleolus-targeting tools, designated pNUTs, to enable rapid and reversible nucleoplasm-to-nucleolus shuttling, with the half-lives ranging from milliseconds to minutes. pNUTs allow both global protein infiltration into nucleoli and local delivery of cargoes into the outermost layer of the nucleolus, the granular component. When coupled with the amyotrophic lateral sclerosis (ALS)-associated C9ORF72 proline/arginine-rich dipeptide repeats, pNUTs allow us to photomanipulate poly-proline–arginine nucleolar localization, perturb nucleolar protein nucleophosmin 1 and suppress nascent protein synthesis. pNUTs thus expand the optogenetic toolbox by permitting light-controllable interrogation of nucleolar functions and precise induction of ALS-associated toxicity in cellular models.

INTRODUCTION

The nucleolus is a prominent membraneless subnuclear structure that is well known to control ribosome biogenesis (1). A typical nucleolus contains three subcompartments in a mammalian cell: the fibrillar center (FC), the dense fibrillar component (DFC) and the outmost granular component (GC), where various steps of ribosome synthesis take place. Mounting evidence indicates that, beyond the control of ribosome biogenesis, the nucleolus also acts as the organizing hub for many functions in health and disease (2). For example, the nucleolus is involved in controlling cell cycle progression (3), response to cellular stress (4,5), virus infection (6) and other essential cellular functions. Indeed, many proteins have been found to localize within the nucleolus and achieve their functions by dynamic shuttling between the nucleolus and the nucleoplasm (7). Some of them have been reported to contain nucleolar localization sequences (NoLSs), which are responsible for cellular trafficking and nucleolar accumulation or retention. Different from nuclear localization sequence (NLS) containing arginine (R)-rich motifs recognized by the importin complex to enable the cytoplasm-to-nucleus transportation of proteins, NoLSs are usually short in size (approximately several to tens of amino acids) composed mostly of R or lysine (K) residues. Most NoLSs do not interact with transporter proteins, but rather physically engage a charge-dependent nucleolus protein or ribosomal RNA (rRNA) (8–10), either directly or indirectly.

Multiple optogenetic and chemogenetic tools have been developed to enable nucleocytoplasmic shuttling and to facilitate the mechanistic probing of nuclear proteins (11–14). In addition, Corelet-based optogenetic tools have been developed for *de novo* liquid–liquid phase separation (LLPS) (15). Corelet has been used as a biomimetic model system to study the composition and thermodynamic interactions of nucleolar components (16), as well as to modulate the liquid-like condensates of telomeres (17). Nonetheless, there is still a need to further expand the repertoire

*To whom correspondence should be addressed. Tel: +1 713 677 7483; Email: yubinzhou@tamu.edu
Correspondence may also be addressed to Lian He. Tel: +1 713 677 7843; Email: lhe@tamu.edu
Correspondence may also be addressed to Peng Tan. Tel: +1 713 677 7483; Email: ptan@broadinstitute.org

of molecular tools tailored for convenient protein delivery and partitioning to specialized subnuclear compartments (18) formed by LLPS (19), including nucleoli (20), nuclear speckles (21), paraspeckles (22), promyelocytic leukemia (PML) bodies (23), Gemini of coiled bodies (Gems) (24) and Cajal bodies (25). Herein, we set out to engineer a set of single-component, photoinducible nucleolar targeting tools (termed as "pNUTs") to enable preferential protein trafficking in and out of nucleolus by light, and to probe the phase separation properties of selected nucleolus-residing proteins that are involved in neurodegenerative diseases, such as amyotrophic lateral sclerosis (ALS). We first fused a light–oxygen–voltage domain (LOV2) (26,27) of *Avena sativa* phototropin 1 with various NoLSs selected from human, mouse, bacterial or viral proteins. We envision that photostimulated conformational changes in LOV2 could unleash caged NoLS and trigger a nucleolar accumulation or retention of the engineered protein. To overcome the limited nucleolar targeting ability of a single NoLS in the LOV2-based pNUTs, we further adopted a light-dependent NoLS polymerization method by fusing a photolyase-homology domain of cryptochrome 2 (CRY2; amino acids 1–498) from *Arabidopsis thaliana* (28,29) with NoLS. We believe that light-induced oligomerization of CRY2 could substantially amplify the nucleolus-targeting signals to promote more efficient nucleolar localization. In parallel, we extended a similar optogenetic engineering strategy to the C9ORF72 dipeptide repeats (DPRs) of poly-proline–arginine (poly-PR), which is tightly associated with ALS due to nucleolar stress and cytotoxicity (30). Here, we optimized a series of CRY2-PR variants, dissected their condensate formation properties and successfully recapitulated their cytotoxicity within the nucleolus in a light-dependent manner. With these tools, we provide the proof of concept to harness the power of light to establish cellular models of ALS-associated poly-PR toxicity, which promises to accelerate the pace of deciphering the pathogenic mechanisms underlying poly-PR-related neurodegeneration.

MATERIALS AND METHODS

Plasmid construction

The standard restriction enzyme digestion–ligation method was used for plasmid construction. KOD Start DNA Polymerase (EMD Millipore, MA, USA) was used for PCR amplification. All the molecular cloning reagents were purchased from New England Biolabs (Ipswich, MA, USA). All the oligos used in this study were synthesized by Integrated DNA Technologies (Coralville, IA, USA) and all constructs were confirmed by Sanger sequencing. For LOV2-NoLS constructs, cDNAs encoding various NoLSs (with a size over 90 bp) were synthesized as gBlock by Integrated DNA Technologies and then subcloned into a pTriEx-mCh-LOV2 backbone vector (31) between the HindIII and XhoI restriction sites. For short NoLS motifs, oligos were ordered, annealed and cloned into the same vector. The LOV2 domain (residues 404–546) was derived from *Avena sativa* phototropin 1. Further mutations in NoLS were introduced by using the QuikChange Lightning Multi Site-Directed Mutagenesis Kit (Agilent Technologies, Santa Clara, CA, USA). For CRY2-NoLS constructs, digested gBlocks or annealed oligos were inserted into the mCh-CRY2 backbone vector (32) between the BspEI and BamHI restriction sites. The CRY2 module was derived from the photolyase-homology region (residues 1–498) of *Arabidopsis thaliana* CRY2. The nucleolar GC maker [GFP-nucleophosmin 1 (NPM1)], DFC marker (mEmerald-fibrillarin-7), FC marker (GFP-UBF) and Gems marker (GFP-SMN) were obtained from Addgene (#17578, #54096, #17656 and #37057; Watertown, MA, USA). The DNA templates encoding other nuclear subcompartment markers were also obtained from Addgene. PCR fragments were amplified and ligated to target vectors by a standard restriction enzyme digestion–ligation cloning method. To generate mCh-LOV2 and mCh-CRY2 controls, the NoLS sequences from pNUT1 and pNUT3 were deleted via standard PCR. The amplified sequence encoding NLS-mCherry (mCh) was digested and ligated to substitute mCh in the mCh-LOV2 plasmid to make NLS-mCh-LOV2, with the nuclear localization signal derived from SV40 T antigen (SV40-NLS: PKKKRKV) induced in the forward PCR primer. A similar strategy was adopted to generate NLS-mCh-CRY2. No additional NLS was used in all constructs, unless otherwise mentioned. The list of plasmid constructs made in the study is summarized in Supplementary Table S1, with the three pNUT plasmids deposited in Addgene (#175744, #175745 and #175746).

Time-lapse confocal imaging, data processing and quantification

A Nikon W1 Yokogawa Spinning Disk confocal with photostimulation microscanner and environmental control incubator was used in this study. To test light-induced nucleolar translocation of mCh-LOV2-NoLS or mCh-CRY2-NoLS constructs, HeLa cells were seeded in 35-mm glass-bottom dishes (D35C4-20-1.5-N; Cellvis, Mountain View, CA, USA) and transfected with individual constructs 20–24 h before imaging. During time-lapse imaging, cells were kept at 37°C with 5% CO_2 using a tightly sealed incubation cage mounted on the fluorescence microscope. Lipofectamine 3000 (Thermo Fisher Scientific, MA, USA) was used for transient transfection following the manufacturer's protocol. In most experiments, the 488-nm laser (at a light power of 0.2 mW for 100 ms) was also the light source to circumvent the need for external blue light-emitting diode (LED). To determine the kinetic parameters of LOV2-NoLS hybrid constructs, images were recorded every 0.5 s for 10 s for both green (excitation: 488 nm; emission: 525 nm) and red channels (excitation: 561 nm; emission: 605 nm). Sequential image acquisition was applied for pulsed stimulation with repeated dark–light cycles. For the dark state, only the red channel was recorded. For the lit state, both red and green channels were used. For CRY2-NoLS constructs, images were taken before (red channel only) and after blue light stimulation (both red and green channels; every 2 s for 1.5 min). For repeated light stimulation, pulsed blue light was applied as indicated in the corresponding figures.

For fluorescence recovery after photobleaching (FRAP) experiments, HeLa cells expressing mCh-CRY2-$(PR)_{13}$

were photobleached in the indicated area and the recovery of fluorescence intensity was measured. An external blue LED (470 nm; 40 $\mu W/mm^2$) was used to keep the protein in the lit state during the whole FRAP process. Spatial control of nucleolar accumulation was achieved by using the FRAP module of the confocal microscope, but the power output was only set at 0.1% (1 ms) to avoid photobleaching. For FRAP measurements, the power output was set at 20% (1 s).

For fluorescence loss in photobleaching (FLIP) experiments, HeLa cells were kept at 37°C with 5% CO_2 and an external blue LED light source (470 nm with a power density of 40 $\mu W/mm^2$) was used to stimulate pNUT nucleolar translocation and maintained through the entire course of FLIP. The 488-nm laser was used in pulsed photobleaching with the power output set at 20% for 1 s. An area of 6 μm^2 was bleached in nucleoplasm with 5-s intervals. Images for mCh-fused nucleolar proteins and pNUTs were collected before and immediately after each bleaching step. The fluorescence intensity in the nucleolus of bleached cells was measured and normalized to the intensity before photobleaching.

To quantify the imaging data, we used the region-of-interest toolbox in the Nikon NIS-Elements software (Minato City, Tokyo, Japan) to define the nucleolar, nucleoplasmic and cytoplasmic regions. The 'Time Measurement' tool was used to determine the fluorescence intensities for mCh-LOV2-NoLS and mCh-CRY2-NoLS variants. The fluorescence intensity ratio (F/F_0 or F_{lit}/F_{dark}) was calculated and plotted as shown in the related figures.

To determine the concentration-dependent oligomerization of CRY2-based pNUT3 and the role of pNUT3 in partitioning or LLPS, fluorescence intensities in the selected nucleolar and nucleoplasmic regions were quantified in a pNUT3 concentration-dependent manner with or without light stimulation. The impact of pNUT3 on the thermodynamics of LLPS was then defined as either the client to the GC phase (single-component homotypic interaction) (16,33) or changing the composition of the nucleolus (composition-dependent heterotypic interactions). For the homotypic model, with increased levels of pNUT3, the nucleoplasmic concentration or intensity remains constant. However, for a heterotypic model, the nucleoplasmic concentration or intensity increases nonlinearly. Linear fits were made by using a 'Simple Linear Regression' function in GraphPad Prism 8.3.0. Ninety-five percent confidence intervals for the regression line are indicated as dashed lines in Figure 2D. Correlation coefficient (r) in Figure 1D was determined using the function of correlation matrix in GraphPad Prism. The net charge for NoLS sequences was calculated by using the online resource: https://pepcalc.com/.

Immunofluorescence staining

HeLa cells were seeded on 35-mm glass-bottom dishes and transfected with mCh-CRY2-$(PR)_n$ variants. Cells were stimulated with pulsed blue light with 1-min ON and 3-min OFF cycles (470 nm, 40 $\mu W/mm^2$) for 1 h, after 24 h of transfection. Cells were then fixed with 4% paraformaldehyde (PFA) for 20 min and then permeabilized with 0.5% Triton X-100 for 10 min at room temperature. After blocking cells with 3% bovine serum albumin (BSA) for 1 h, an anti-NPM1 monoclonal antibody (clone NA24 at 1:100 dilution; Thermo Fisher Scientific, Waltham, MA, USA) was added to cells and incubated at 4°C overnight. The secondary goat anti-mouse Alexa Fluor 488 IgG (A-11029 at 1:1000 dilution; Thermo Fisher Scientific, Waltham, MA, USA) was used to label the primary NPM1 antibody at room temperature for 1 h. Phosphate-buffered saline (PBS) washing was repeated three times after each step's solution change.

To detect puromycylation of newly synthesized polypeptides, cells transfected with mCh-CRY2-$(PR)_n$ variants were incubated with 5 $\mu g/ml$ puromycin (P8833; Sigma-Aldrich, St. Louis, MO, USA) for 10 min in the absence or presence of pulsed light stimulation as described earlier. Cells were then washed with PBS three times and fixed with 4% PFA for 20 min, followed by permeabilization with 0.5% Triton X-100 for 10 min and blocked with the blocking buffer (3% BSA in PBS) for 1 h. A primary anti-puromycin antibody (EQ0001, 1:1000; Kerafast, Boston, MA, USA) was added to the blocking buffer and incubated overnight at 4°C. Sixteen hours later, anti-mouse Alexa Fluor 488 IgG (A-11029, 1:1000;Thermo Fisher Scientific, Waltham, MA, USA) was added and incubated with cells for 1 h at room temperature, followed by three times of PBS wash to minimize unspecific binding.

Fluorescence *in situ* hybridization

The fluorescence *in situ* hybridization (FISH) for nucleolar pre-RNA was carried out as described (34). A probe spanning the 18S-internal transcribed spacer 1 (18S-ITS1) junction (5′ITS1: 5′-CCTCGCCCTCCGGGCTCCGTTA ATGATC-3′) was conjugated in its 5′-end to FAM and used for the FISH experiment. The transfected cells grown on four-chamber glass-bottom dishes were treated with or without blue light pulse (470 nm, 40 $\mu W/mm^2$, 1-min ON and 3-min OFF cycles for 1 h), then washed twice with PBS and fixed with 4% PFA in PBS for 30 min. Next, cells were permeabilized with 0.5% Triton X-100 for 5 min, followed by subsequent two washes with 2× SSC containing 10% formamide. Cells were incubated with a hybridization buffer (10% formamide, 2.1× SSC, 0.5 $\mu g/ml$ rRNA, 10% dextran sulfate, 250 $\mu g/ml$ BSA, 10 mM ribonucleoside vanadyl complexes, 0.5 $ng/\mu l$ probe) at 37°C in the dark for at least 5 h. Cells were ready for imaging after two washes with 2× SSC (with 10% formamide) at 37°C. For data analysis, the 5′ITS1 staining intensity for mCh-positive cells was normalized to the signals from mCh-negative cells.

CRISPR-mediated knock-in of an mCh tag to HNRNPA1

Endogenous mCh tag knock-in for the nuclear protein heterogeneous nuclear ribonucleoprotein A1 (HNRNPA1) was carried out as described in Fueller *et al.*'s study (35). Primers containing HNRNPA1 homology arms and other necessary components were used to amplify the mCh cassette (pMaCTag-13, Addgene #119992). HNRNPA1-M1 tagging oligo: 5′-AAAGAAAAATTGTACTTTTCAGGTGGCTATGG CGGTTCCAGCAGCAGCAGTAGCTATGGCAGTG

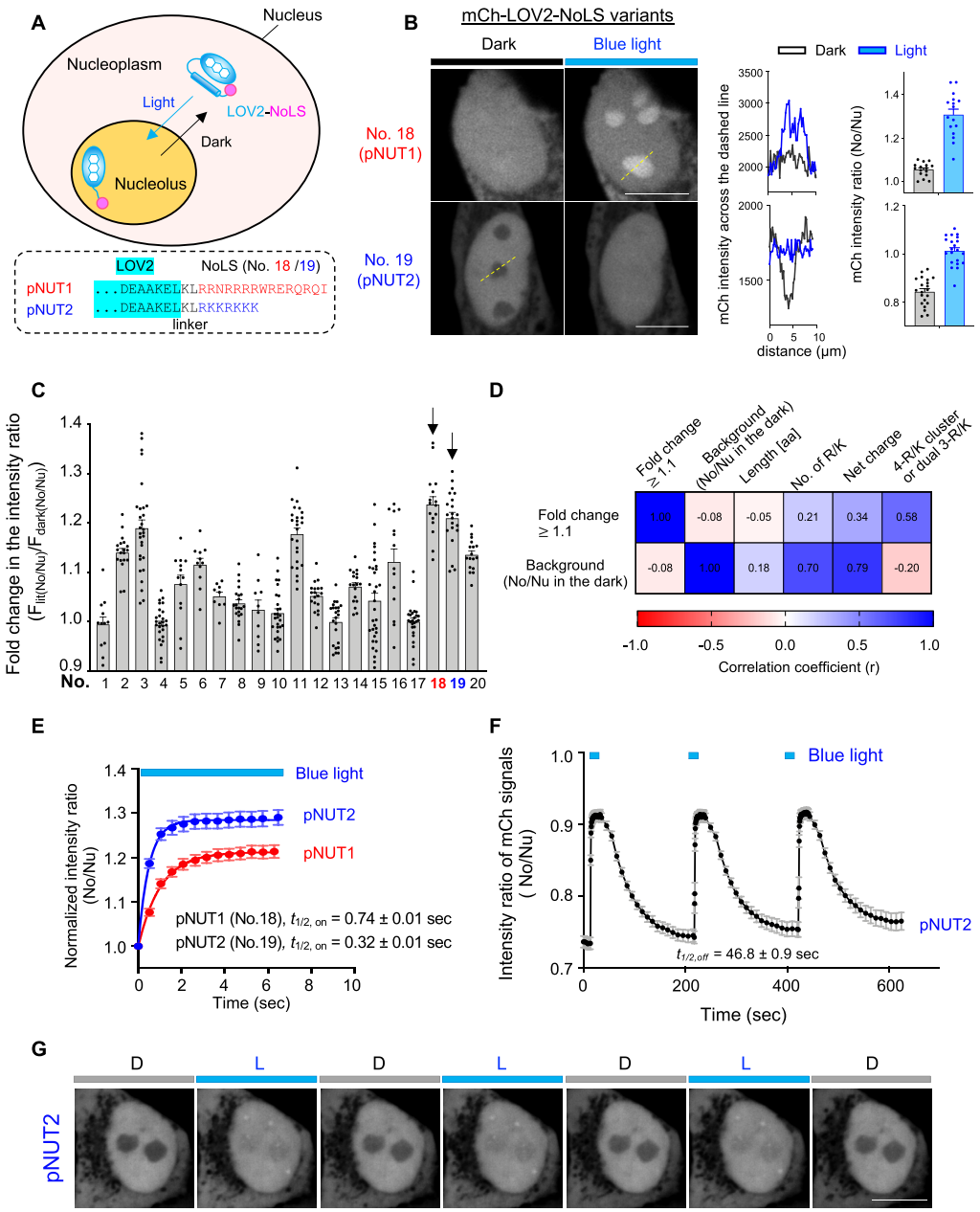

Figure 1. Design and characterization of LOV2-based pNUTs. (**A**) Schematic depiction of the design. Twenty putative NoLSs derived from various species (see Supplementary Table S2) were individually fused to the C-terminus of LOV2 to yield LOV2-NoLS hybrid proteins. In the dark, the NoLS motif is predominantly masked presumably by docking toward the LOV2 core domain. After blue light stimulation, light-induced structural changes in LOV2 cause rapid unfolding of the C-terminal Jα helix, thereby exposing NoLS to restore its nucleolar targeting capability. No. 18 (red) and No. 19 (blue) show the most prominent changes upon light illumination with the least background activation and are named as pNUT1 and pNUT2, respectively. The primary sequences for the junction regions between LOV2 and NoLS are shown below the cartoon. (**B**) Representative confocal images of HeLa cells expressing mCh-LOV2-NoLS before (dark) and after light illumination for 10 s (470 nm). Two LOV2-NoLS variants (No. 18 and No. 19) are shown as typical examples. Fluorescence intensity profiles and light-induced changes in the fluorescence intensity [quantified as the nucleolus/nucleoplasm (or No/Nu) intensity ratio of mCh fluorescence] across the yellow dashed line are shown on the right. Scale bar, 10 μm. $n = 16$–21 cells from three independent experiments. Error bars denote standard error of the mean (s.e.m.). (**C**) Quantification of light-dependent responses (as the No/Nu ratio) of mCh-LOV2-NoLS variants. Lit, light stimulation. $n = 12$–29 cells. Data are shown as mean ± s.e.m. Also see Supplementary Figures S2 and S3 for representative images and detailed quantification (dark *versus* light) for each construct. (**D**) Evaluation of the correlation among the indicated parameters. Light-induced fold change in the No/Nu intensity ratio of mCh (No/Nu > 1.1 as a cutoff) showed a significant positive correlation with the presence of 4-R/K or dual 3-R/K clusters in NoLS motifs ($r = 0.58$). The background nucleolar partition (in the dark) was positively correlated with the numbers of R/K residues ($r = 0.70$), as well as the net charge ($r = 0.79$). The scale bar indicates the correlation coefficient from low (red) to high (blue). Also see Supplementary Figure S3. (**E**) Light-induced changes in normalized No/Nu ratio of mCh-pNUT1 and mCh-pNUT2 when expressed in HeLa cells. The activation half-lives are indicated below the curves. $n = 18$–23 cells (mean ± s.e.m.). (**E**) Quantification of the No/Nu ratio of mCh-pNUT2 in response to three repeated dark–light cycles. $n = 52$ cells. (**G**) Representative confocal images showing reversible translocation of mCh-pNUT2 between nucleoplasm and nucleolus in live HeLa cells. Three repeated dark–light cycles of stimulation were applied. Scale bar, 10 μm. Also see Supplementary Movie S2. See Supplementary Figure S5 and Supplementary Movie S1 for the performance of mCh-pNUT1.

GCAGAAGATTTTCAGGTGGAGGAGGTAGTG-3′; HNRNPA1-M2 tagging oligo: 5′-TTTAAAAAATTA TGTCAACACACAAAAAGGTGCTTACTTACCTA AaaaaaaAAGGTGCTTACTTACCTAATatctacactta gtagaaattaGCTAGCTGCATCGGTACC-3′. The PCR product was separated by agarose gel electrophoresis and purified by column purification, and then cotransfected with Cas12a [pcDNA3.1-hLbCpf1 (TYCV) (pY230), Addgene #89355] into HeLa cells. For each well in a 24-well plate, 500 ng PCR product and 500 ng Cas12a were used for transfection. Seventy-two hours after transfection, mCh-positive cells were sorted by flow cytometry. The expression levels of pNUT1–3 (200 ng/well for pNUT1 and pNUT2 and 500 ng/well for pNUT3 in 24-well plates were used) relative to endogenous nuclear protein were determined by CRISPR-mediated mCh knock-in in frame with a known nuclear protein encoded by *HNRNPA1* (HNRNPA1-mCh). pNUT1 and pNUT2 showed ∼3-fold higher expression than endogenous HNRNPA1, while pNUT3 was expressed at a similar level to endogenous HNRNPA1 (Supplementary Figure S1).

Cell proliferation and cell cycle assays

To monitor cell proliferation, HeLa cells were seeded in 24-well plates at a density of 10^5 cells/well. One plate was kept in the dark and the other was subjected to pulsed blue light illumination (470 nm, 40 μW/mm^2 with 1-min ON and 3-min OFF cycles; Thorlabs, Newton, NJ, USA). Cells were collected and cell numbers were counted by a TC20 automated cell counter (Bio-Rad Laboratories, Hercules, CA, USA) at 24, 48 and 72 h after seeding. The cells were washed twice with PBS and fixed with 4% PFA for 20 min. Next, fixed cells were washed twice with PBS and kept at 4°C. After all the samples were collected, cells were stained with a DAPI working solution (2 μg/ml DAPI, 0.1% Triton X-100 in PBS) for 10 min in the dark. Cell suspensions were analyzed by an LSRII cytometer (BD Biosciences, Franklin Lakes, NJ, USA). BD FACSDiva (Franklin Lakes, NJ, USA) and FlowJo (Ashland, OR, USA) software were used for data collection and analysis.

Statistical analysis

GraphPad Prism 8.3.0 software was used to plot the data and all the data were shown as mean ± s.e.m., unless otherwise noted. The sample size is indicated in the figure legends for each experiment. Half-lives were determined by using a single-component exponential decay function. Statistical analysis was performed using unpaired Student's *t*-test: $^{*}P < 0.05$, $^{**}P < 0.01$, $^{***}P < 0.001$ and $^{****}P < 0.0001$.

RESULTS

Design and optimization of pNUTs for photoactivatable nucleolar targeting

To create a light-inducible nucleolar localization signal, we took advantage of the LOV2 domain of *Avena sativa* phototropin 1 (AsLOV2) to photocage a putative NoLS (36). When appended downstream of the C-terminal Jα helix of the AsLOV2 domain, the NoLS is concealed from the nucleolus import machinery in the dark state (Figure 1A). Upon blue light stimulation, the Jα helix unfolds and undocks from the LOV2 core domain, allowing the NoLS to be exposed for nucleolar targeting (Figure 1A). Hence, we envision that the engineered LOV2-NoLS can be used to tag and regulate the nucleolar translocation of a given protein via light. By selecting 20 validated or putative NoLS sequences derived from different species (Supplementary Table S2) (10,37), we generated 20 LOV2-NoLS hybrid constructs and assessed their subnuclear localization before and after light illumination (Supplementary Figures S2 and S3). We termed these hybrid constructs as pNUTs. Positively charged peptide entities (arginine and lysine) could interact with nucleolar RNAs or proteins that facilitate the accumulation of NoLS-containing proteins in the nucleoli. To quantitatively evaluate the degrees of nucleolar accumulation with fluorescence microscopy, we fused each pNUT variant to the monomeric red fluorescent protein mCh and compared the nucleolus-to-nucleoplasm (No/Nu) intensity ratio of mCh in the dark and lit states in HeLa cells (Figure 1B and C; Supplementary Figures S2 and S3). In the dark state, 50% of engineered LOV2-NoLS hybrid proteins were primarily excluded from the nucleolus (Nos 1, 5, 9, 10, 12, 15, 16, 17, 19 and 20 with a ratio <1). For the remaining half constructs, four exhibited even distribution throughout the nucleus (Nos 2, 3, 4 and 18 with a ratio = 1) and six showed overt pre-accumulation in the nucleoli (Nos 6, 7, 8, 11, 13 and 14 with a ratio >1; Supplementary Figures S2 and S3). Upon light illumination, 8 out of 20 (Nos. 2, 3, 6, 11, 16, 18-20) showed statistically significant nucleoplasm-to-nucleolus translocation (Figure 1C, intensity ratio >1; Supplementary Figures S2 and S3, highlighted in green). No. 18 and No. 19 showed the most prominent changes upon light illumination without overt background activation, and were hereafter named as pNUT1 (NoLS: RRNRRRRWRERQRQI from the HIV Rev transactivating protein) and pNUT2 (RKKKRKKK from human nuclear factor-κB inducing kinase), respectively (Figure 1B and C).

Based on these findings of distinct targeting efficiency and dark activity among various NoLSs, we set out to study the nucleolar recruitment principles of LOV2-based pNUTs. By analyzing the correlation between the patterns in NoLS motifs (including net charge, number of arginine and lysine residues, and sequence length) and the nucleolar targeting efficiency, we found that the recruitment activity was positively correlated with the number of continuous positively charged R/K residues within NoLS, while the dark activity (high background without light stimulation) was positively correlated with the number of R/K residues or the net charge. Notably, NoLS with four continuous positively charged R or K combinations (4-R/K cluster) or with two copies of triple R/K (3-R/K cluster) showed the greatest fold change with the exception of NoLS No. 19 (RKKRKKK), probably due to its shorter length but higher net charge (Figure 1D; Supplementary Figure S3B and C). To validate this finding, we individually introduced 4-R/K cluster via site-directed mutagenesis in NoLS motifs with poor/no nucleolar targeting (Nos 1, 4, 5, 7, 8, 9, 10, 12, 13, 14, 15 and 17; numbers followed by an 'm' represent the corresponding mutants) and monitored their

nucleolar targeting efficiency (mCh intensity ratio; No/Nu) before and after light stimulation. Ten out of the 12 tested mutants with 4-R/K clusters indeed showed varying degrees of improvement in nucleolar recruitment (Supplementary Figures S3B and S4). Our findings suggest that positively charged polypeptides bearing 4-R/K clusters have a strong tendency for nucleolar targeting, which can be coupled with LOV2 to enable light-inducible nucleolar recruitment of proteins of interest.

When expressed in HeLa cells, pNUT1 showed a smooth nuclear distribution in the dark and exhibited >23% increase in nucleolus/nucleoplasm signals. By comparison, pNUT2 was excluded from the nucleolus in the dark and displayed nearly 20% gain in the nucleolus/nucleoplasm signals in response to photostimulation (Figure 1B). Both pNUTs exhibited rapid activation kinetics, with the half-lives determined to be 740 ms for pNUT1 and 320 ms for pNUT2 (Figure 1E). Importantly, light-induced nucleolar translocation of pNUT1 or pNUT2 could be fully reversed without compromising the activation/deactivation amplitude by switching off the light source, with the deactivation half-lives falling in the range of 40–50 s (pNUT1, 43.4 ± 1.5 s; pNUT2, 46.8 ± 0.9 s; Figure 1F and G; Supplementary Figure S5, Supplementary Table S3 and Supplementary Movies S1 and S2). Collectively, we have engineered a set of LOV2-NoLS hybrid constructs that predominantly target nucleoli in a light-dependent manner with fast kinetics.

In addition to tight colocalization with nucleolar markers, ∼30% of pNUT2-expressing cells also showed light-induced non-nucleolar accumulations or aggregates in the nucleoplasm (Figure 1G; small puncta), which partially colocalized with selected nuclear subcompartments, including PML bodies marked by mEmerald-PML-IV and Cajal bodies indicated by GFP-coilin (Supplementary Figure S6). However, no overt colocalization was noted with other subnuclear structures, such as nuclear speckles (indicated by SC-35-GFP), paraspeckles (GFP-NONO), heterochromatin (mEmerald-HP1a) and Gems (GFP-SMN; Supplementary Figure S6).

CRY2-based pNUTs for light-inducible translocation into nucleolar subcompartments

LOV2-based pNUTs succeeded in translocating a target protein bearing a single NoLS. However, to trigger a cellular event often requires the concentration of signaling molecules to reach a threshold [such as oligomerization of innate immune sensing molecules (38,39) and initiation of phase separation (40)]. We set out to further diversify the pNUT system to induce a higher nucleolar load of proteins or protein complexes by light. To explore this idea, we replaced the LOV2 domain in all the 20 LOV2-NoLS variants with the photolyase-homology domain of CRY2 (residues 1–498), which is known for its use in light-inducible protein clustering (41). We next examined whether oligomerization of NoLS could induce nucleolar translocation of a target protein (Figure 2A), and if any, its specific location in the nucleolar subcompartments (Figure 2B). The entire liquid-like membraneless nucleolus comprises different nucleolar compartments and a large number of nucleolar proteins (7) that are distinct in miscibility that keep the compartments phase separated (42), including the DFC that contains fibrillarin (FIB1) and is critical for processing the nascent rRNAs emerged from the FC containing RNA polymerase I for transcription of rRNA, whereas the GC contains NPM1, which is involved in ribosome biogenesis. After screening 20 mCh-CRY2-NoLS fusion constructs, we found that No.19 stood out as the best candidate (hence named as pNUT3), which showed the least background nucleolar accumulation but a high dynamic change (over 2-fold) when compared to No. 18 (with higher dark activity) under the lit condition (Figure 2B and C; Supplementary Figures S7 and S8). Upon light illumination, we visualized rapid translocation of mCh-pNUT3 into the intranucleolar GC region, as evidenced by its tight colocalization with GFP-NPM1 (a GC marker) but not with mEmerald-fibrillarin (a DFC marker) (Figure 2B).

CRY2 has been used to photoinduce oligomerization of intrinsically disordered proteins (IDPs) (33) and to promote single-component LLPS at a fixed saturation concentration (C_{sat}) (16). In contrast, NPM1 or multivalent proteins containing polyarginine motifs such as surfeit locus protein 6 (SURF6) has been reported to be involved in LLPS through heterotypic multicomponent interactions that fit into a concentration-dependent thermodynamically stabilized model: a nonlinear increase in dilute phase concentration (nucleoplasmic concentration) at higher overexpression of NPM1 or SURF6 (16). We next determined whether these CRY2-based constructs are involved in nucleolar partitioning or LLPS by examining the correlation between the concentration of our construct and the fold recruitment into the nucleolus. If CRY2-based pNUTs (with pNUT3 as a test case) have an impact on GC LLPS, we expect to see a less fold recruitment into nucleolus and increased nucleoplasmic concentration at higher expression levels. The average concentration for each construct was tested as indicated by the mean mCh fluorescence intensity. However, no significant correlation between concentration and fold recruitment into the nucleolus was observed. For example, constructs 2, 11 or 14 showed high fold nucleolus recruitment but low in concentrations (∼500 a.u.), whereas constructs 18 or 19 also showed high fold change but higher in concentrations (∼2000 a.u.) (Figure 2C; Supplementary Figure S8). We further evaluated how pNUT3 concentration (indicated by mCh intensity) affects its relative partitioning in nucleolus and nucleoplasm upon light stimulation. We observed increased levels of pNUT3 in both nucleolus (fold recruitment and oligomerization) (Figure 2D, left) and nucleoplasm (Figure 2D, right) at increasing expression levels without saturation. This trend seems to be different from the reported behaviors of NPM1 and SURF6 when overexpressed in mammalian cells, in which both underwent phase separation and had less fold recruitment into the nucleolus at higher level of expression. These results suggest that pNUT3 does not seem to impact GC LLPS but behaves more like a client protein partitioning into the nucleolus (16).

Given the high spatial precision of light, we further tested the use of localized photostimulation to sequentially trigger the nucleolar delivery of mCh-pNUT3 expressed in two neighboring cells (Figure 2E; Supplementary Movie S3).

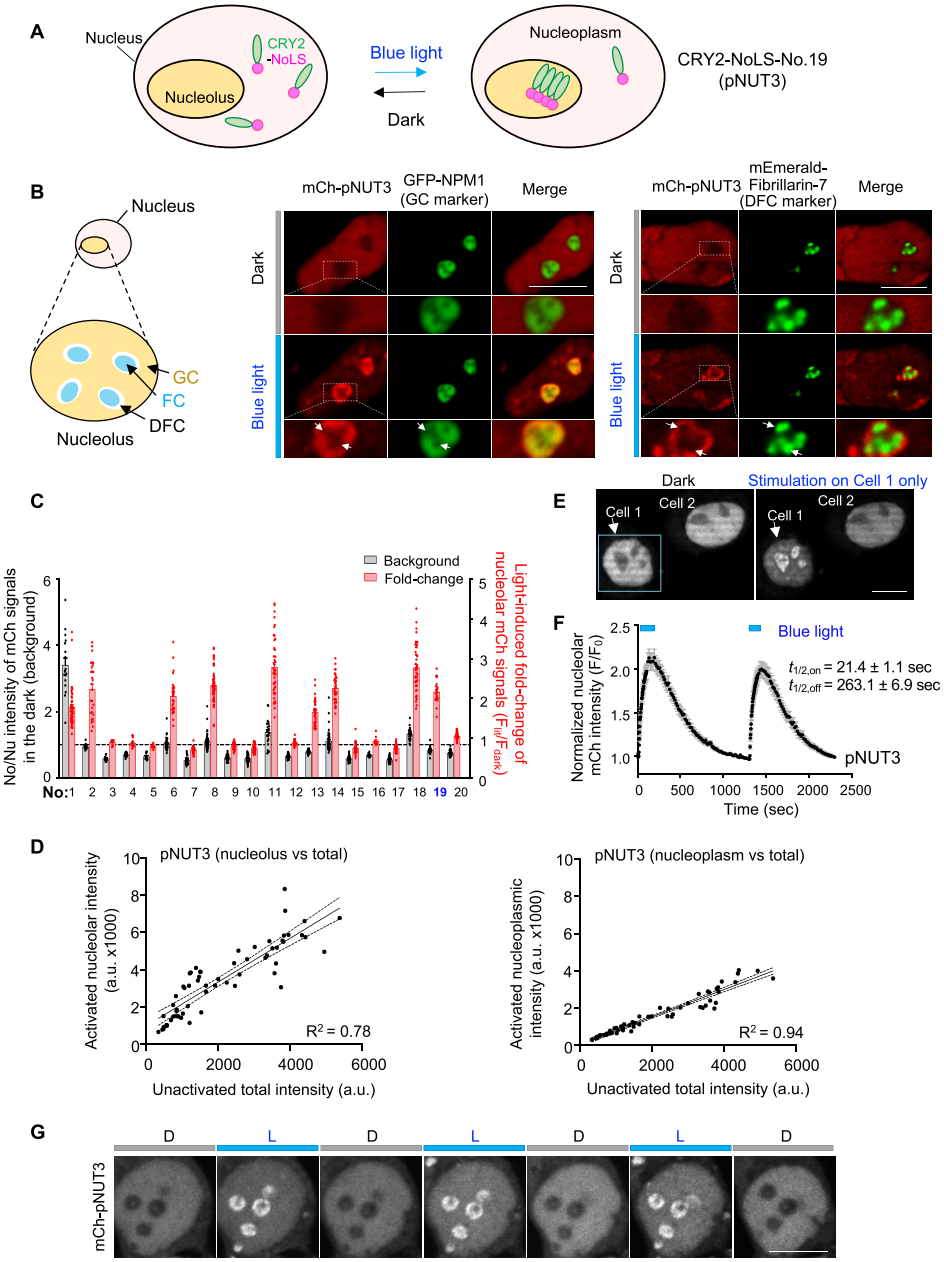

Figure 2. Engineering CRY2-based pNUTs for light-inducible translocation into nucleolar subcompartments. (**A**) Diagram showing the use of light-inducible oligomerization of NoLS to boost nucleolar targeting. An NoLS (e.g. No. 19) was fused to the photosensory photolyase-homology domain of CRY2 to yield CRY2-NoLS hybrid proteins. Upon blue light illumination, CRY2 undergoes oligomerization to increase the NoLS avidity to promote the translocation toward the nucleolus. Construct No. 19 showed a relatively high degree of nucleolar targeting (designated pNUT3). (**B**) mCh-pNUT3 exhibited light-dependent translocation into the nucleolar subdomain GC (marked by GFP-NPM1) but not DFC (indicated by mEmerald-fibrillarin-7). Left panel: a schematic illustration of three subcompartments within a nucleolus: the FC, the DFC, and the GC. Middle and right panels: subnuclear localization of mCh-CRY2-No.19 (designated pNUT3). Representative confocal images of HeLa cells, cotransfected with mCh-pNUT3 and the GC marker GFP-NPM1 (middle) or DFC marker mEmerald-fibrillarin-7 (right), are shown. Zoomed-in views of boxed areas are shown below the corresponding images. White arrow indicates the exclusion of mCh-pNUT3 from DFC regions marked by mEmerald-fibrillarin-7. Scale bar, 10 μm. (**C**) Quantification and comparison of mCh-CRY2-NoLS constructs for their degrees of background nucleolar localization (quantified by the No/Nu intensity ratio in the dark) and ranges of dynamic changes included by light (quantified by the fold change of nucleolar mCh signals). Also see Supplementary Figure S7 for representative images for each construct. (**D**) Correlation between the mCh intensity (a.u. ×1000) in the nucleolus (left) or nucleoplasm (right) after light activation (*Y*-axis, activated nucleolar mCh intensity) and the total intensity at increasing expression levels (*X*-axis, total mCh intensity prior to photoactivation). The data fit to a linear correlation for pNUT3 with an increasing expression level. $n = 61$ cells. Solid and dashed lines represent the linear fit and 95% confident intervals, respectively. (**E**) Spatial control over the nucleolar targeting of mCh-pNUT3 in live cells. Photostimulation was applied to the selected area that contained Cell 1 (indicated by a blue box) but not Cell 2. Also see Supplementary Movie S3. (**F**) Quantification of changes in the nucleolar intensity of mCh-pNUT3 in response to two repeated dark–light cycles. $n = 28$ cells (mean ± s.e.m.). See Supplementary Figure S8 and Supplementary Table S3 for the overall summary of activation and deactivation half-lives for all constructs. (**G**) Representative confocal images showing reversible control over the nucleolar targeting of mCh-pNUT3. HeLa cells expressing mCh-pNUT3 were subjected to three repeated dark–light stimulation cycles. Scale bar, 10 μm.

We found that only the cell under direct light illumination exhibited noticeable nucleolar translocation, thus establishing the feasibility of applying pNUTs for spatial control of protein localization in the nucleolus within living cells. Similar to LOV2-based pNUTs, the nucleolar translocation of pNUT3 from the nucleoplasm could be fully reversed, with the activation and deactivation half-lives determined to be 21.4 ± 1.1 and 263.1 ± 6.9 s, respectively (Figure 2F and G; Supplementary Movie S4 and Supplementary Table S3). Interestingly, in some cells, the light-activated pNUT3 exhibited partial colocalization with fluorescent markers that stain PML bodies (mEmerald-PML-IV), nuclear speckles (SC-35-GFP) and Gems (GFP-SMN) (Supplementary Figure S9). To examine whether such non-nucleolar aggregates were caused by CRY2 itself, we examined the colocalization of mCh-CRY2 with 10 subnuclear markers. Indeed, CRY2 itself was found to colocalize with markers residing in PML bodies and nuclear speckles (43), but not with Gems (Supplementary Figure S10). Taken together, we have illustrated the use of CRY2-based pNUT3 for efficient photoswitchable delivery of proteins primarily to the subnucleolar GC region with high spatiotemporal precision.

After screening 40 optogenetic constructs by fusing NoLS with either LOV2 (photoinducible uncaging) or CRY2 (light-induced oligomerization) with pulsed blue light (low power with no cell damage or adverse changes in cell cycle), we identified at least three candidates (pNUT1, pNUT2, and pNUT3) showing robust changes in nucleolar trafficking with varying kinetics in response to light stimulation (Supplementary Figure S11 and Supplementary Table S3). Notably, in the dark, CRY2-based pNUT3 (mCh-pNUT3) showed notable nuclear localization with a nucleus-to-cytosol intensity ratio similar to that of NLS-mCh-CRY2. LOV2-based pNUT1 or pNUT2 also showed partial accumulation within the nuclei even in the absence of light stimulation. These results suggest that NoLS to some extent acts as NLS to promote nuclear translocation in the dark (Supplementary Figure S12A and B). If comparing mCh intensities in the nucleoplasm and cytoplasm before and after light stimulation (F_{lit}/F_{dark}), we observed a decrease of mCh intensity ratio in the nucleoplasm (i.e. <1) but no change in the cytoplasm (i.e. ∼1), suggesting that pNUT1–3 mainly promoted nucleoplasm-to-nucleolus shuttling, but not cytoplasm-to-nucleus shuttling (Supplementary Figure S12C).

To further characterize the mobility of the pNUTs, we carried out a fluorescence loss in photobleaching (FLIP) experiment in the nucleolus and determined the fluorescence decay rates of pNUTs and representative nucleolar proteins, such as NPM1, fibrillarin-7 and UBF (Figure 3). pNUT1 and pNUT2 showed a relatively rapid rate of fluorescence decay from the nucleoli with the half-lives ($t_{1/2}$) determined to be 28.3 ± 4.4 s (pNUT1) and 27.5 ± 5.5 s (pNUT2). In contrast, pNUT3 displayed much slower kinetics ($t_{1/2}$ = 206.8 ± 7.5 s), indicating a longer retention time of pNUT3 in the nucleolus or the oligomerized molecules in the nucleoplasm failing to exchange sufficiently. These results suggest that pNUT1 and pNUT12 are highly mobile in the nucleus, whereas pNUT3 tends to be retained in the nucleolus or frozen at an oligomerization state. Unlike optoDroplet-mediated reversible oligomerization of IDR (intrinsically disordered repeat)-containing ribonucleoprotein body proteins and phase separation throughout the cytosol and nucleoplasm (44), our LOV2- or CRY2-based pNUTs enable reversible, versatile and user-defined protein delivery to nuclear subcompartments that are important for modulating the dynamics and functions of nuclear condensates.

Light-tunable nucleolar partitioning of ALS-associated DPRs

Having succeeded in devising pNUTs with native NoLS motifs derived from humans and viruses, we extended our engineering strategy to pathogenic NoLS-like motifs that are associated with human disease. Repeat expansion in the *C9ORF72* gene is known to be associated with neurodegenerative disorders, including ALS and frontotemporal dementia (FTD). The unconventional translational products of C9ORF72, made of arginine-rich DPRs such as poly-PR, have been shown to undergo dynamic phase separation in the nucleolus (45). Poly-PR could further inhibit the ribosome's peptidyl transferase activity (46) and disrupt the proper phase separation of NPM1, a key protein involved in organizing ribosomal proteins and RNAs within the nucleolus (47). Inspired by the nucleolar targeting of pNUT3, we fused mCh-CRY2 with poly-PR variants bearing 5–37 copies of DPR and measured their degrees of nucleolar localization before and after light stimulation (Figure 4A and B). In the dark, when the DPR number exceeded 19, we were able to see a dominant localization of the hybrid protein within the nucleoli with condensate formation reminiscent of LLPS. Under the lit condition, we started to discern clear nucleolar translocation and oligomerization of the engineered mCh-CRY2-$(PR)_n$ variants with nine or more DPRs. Given that CRY2 in the lit condition exists at least as a dimer, we believe that at least 18–20 DPRs are required for efficient nucleolar partitioning and the formation of liquid-like condensates. Moreover, light-induced nucleolar phase separation of mCh-CRY2-$(PR)_n$ could be readily reversed upon withdrawal of light, with the activation kinetics in the range of 16–34 s and the deactivation half-lives falling between 2.5 and 7.1 min (Figure 4C; Supplementary Table S3). Notably, light-triggered differential partition in nucleoli and the nuclear speckles was observed in cells expressing mCh-CRY2-$(PR)_n$. For variants with <11 DPRs, we observed a largely positive correlation between nucleolar accumulation and the DPR length (Figure 4B), but an inverse relationship between the degree of nuclear speckle aggregation and the DPR number (Figure 4D and E; Supplementary Figure S13). When the repeat number exceeded 12, we noted a predominant nucleolar distribution of mCh-CRY2-$(PR)_n$ (Figure 4A and D; Supplementary Figure S13). These results suggest the differential partitioning of poly-PR in a light- and dipeptide length-dependent manner.

In parallel, we applied FRAP (48) to determine the molecular dynamics and mobility of the mCh-CRY2-$(PR)_{13}$ condensates when exposed to light stimulation. The mCh-CRY2-$(PR)_{13}$ showed a half-time of 53.8 ± 6.6 s for fluorescence recovery (Figure 4F and G), indicating a rela-

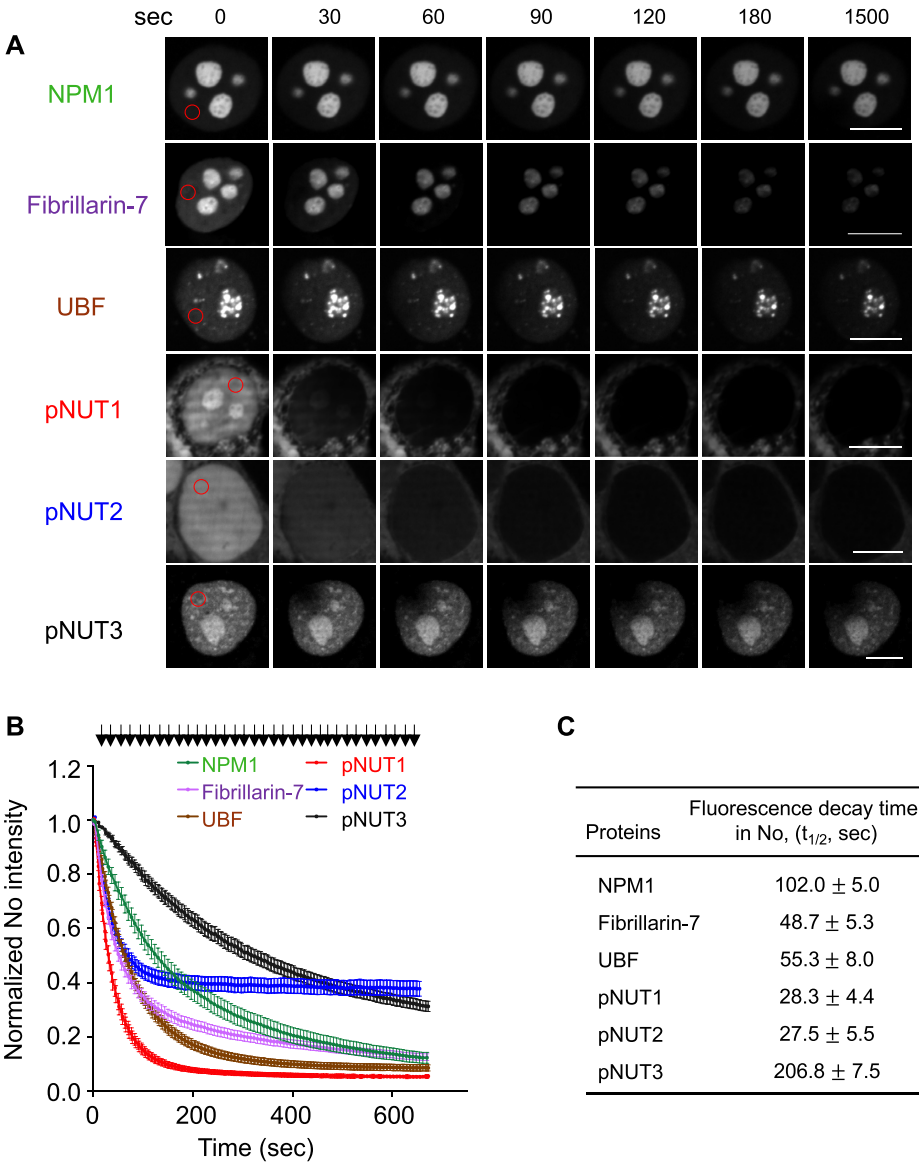

Figure 3. Assessing the pNUT mobility by FLIP. (**A**) Representative confocal images for FLIP experiments to assess the difference in mobility of pNUTs and nucleolar proteins in transit between the nucleolus (No) and nucleoplasm (Nu) in HeLa cells. External blue light was applied to photoactivate pNUTs and maintained through the entire course of FLIP. Red circles indicate the areas of repeated photobleaching. The cumulative bleaching duration is shown above the images. Scale bar, 10 μm. (**B**) The loss of fluorescence signal in the nucleoli was measured over time. pNUT1 and pNUT2 exit the nucleolus faster than nucleolar proteins, such as NPM1, fibrillarin-7 and UBF, while pNUT3 showed a substantially slower decay rate. Arrows indicate the photobleaching events. Data are shown as mean ± s.e.m. (n = 16–39 cells). (**C**) A summary of nucleolar retention half-time for proteins examined in panel (B).

tively high condensate fluidity (49) (comparable to NPM1 with a half-time of 64 s), as well as the high feasibility of optogenetic mimicry of C9ORF72-DPR-mediated nucleolar condensate formation *in cellulo*. Taken together, photoinduced oligomerization of positively charged DPRs can be exploited for conditional protein delivery into the nucleoli, as well as induction of nucleolar condensates by using light. More importantly, the optogenetic engineering approach enables us to identify the minimal assembly units required for effective nucleolar targeting and phase separation of ALS/FTD-associated poly-PR derived from C9ORF72.

Light-inducible poly-PR nucleolar infiltration to mimic ALS-associated DPR toxicity

We moved on to test whether the light-inducible nucleolar accumulation of CRY2-$(PR)_n$ could be exploited to perturb nucleolar functions, by using the endogenous phase separation of nucleolar NPM1 and ribosomal activity (42,46) as two independent readouts (Figure 5). Through multivalent interactions with proteins with arginine-rich linear motifs and rRNA, NPM1 can undergo phase separation into liquid-like droplets and act as a critical contributor to the liquid-like properties of the GC region of the nucleolus (42,50). We reasoned that light-inducible nucleolar in-

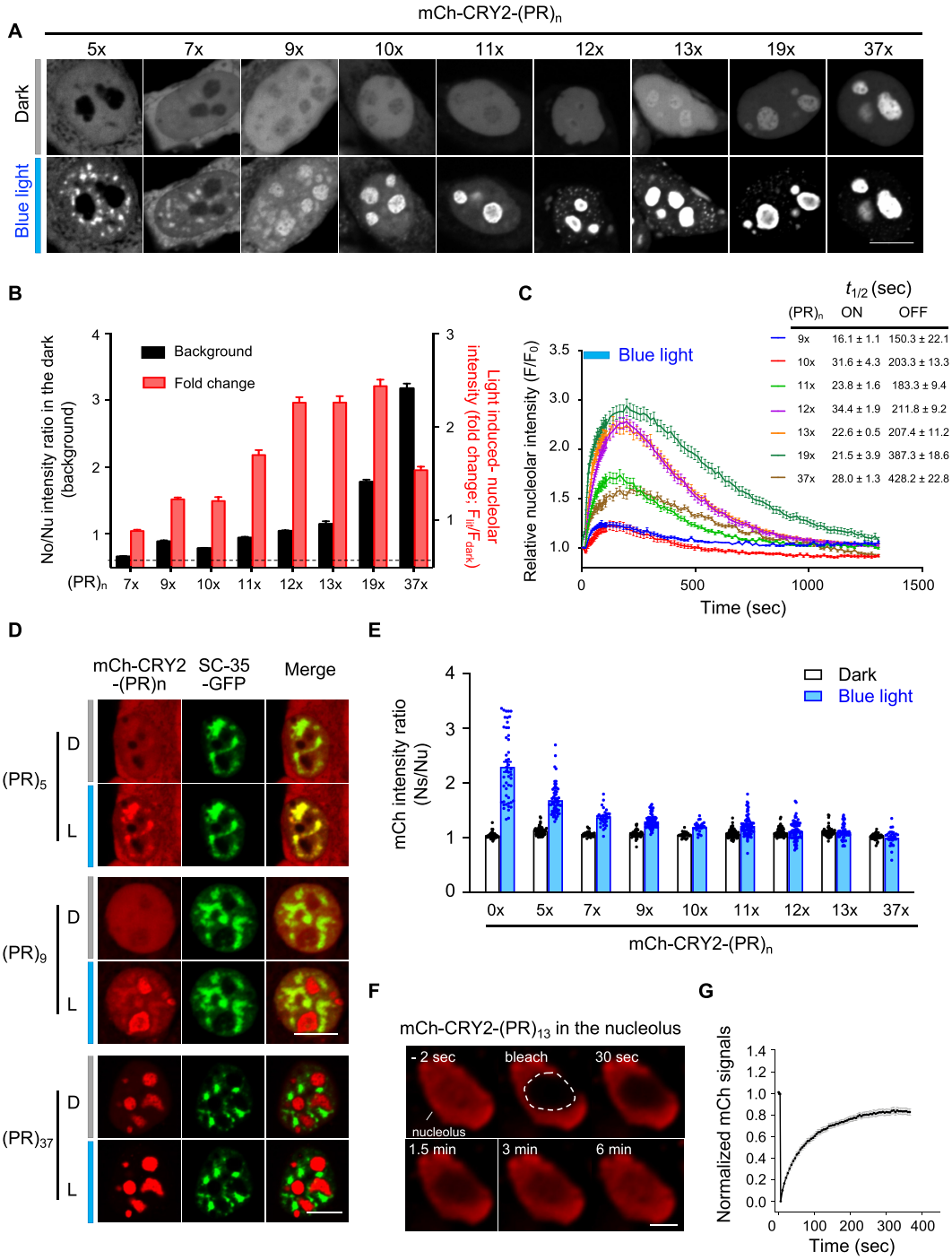

Figure 4. Light-tunable nucleolar accumulation and condensate formation of C9ORF72 poly-PR. (**A**) Representative confocal images of HeLa cells expressing mCh-CRY2-(PR)$_n$ variants before and after light stimulation. Poly-PR DPRs with varying lengths (5–37 repeats) were fused with CRY2 and transiently expressed in HeLa cells. Scale bar, 10 μm. (**B**) Quantification and comparison of the background nucleolar signals (No/Nu ratio in the dark state) and the fold change of nucleolar signals for mCh-CRY2-(PR)$_n$ variants. n = 24–60 cells (mean ± s.e.m.). (**C**) Time course showing light-induced nucleolar translocation kinetics of mCh-CRY2-(PR)$_n$ variants. The process could be fully reversed upon withdrawal of light. The activation half-lives were in the range of 16–34 s, whereas the deactivation half-time fell between 150 and 428 s. n = 31–60 cells (mean ± s.e.m.). (**D**) Confocal images of HeLa cells co-expressing mCh-CRY2-(PR)$_n$ and the nuclear speckle marker SC35-GFP. Upon light stimulation, less mCh-CRY2-(PR)$_n$ was found to colocalize with nuclear speckles (SC-35-GFP) when the length of PR repeats increased. Scale bar, 10 μm. (**E**) Qualification data to demonstrate the relationship between nuclear speckle accumulation and the number of PR repeats before (white bar) and after light stimulation (blue bar). The ratio of nuclear speckle (Ns) over nucleoplasm (Nu) signals (Ns/Nu) was used to indicate the degree of nuclear speckle accumulation. Also see Supplementary Figure S13 for more images. (**F**) Representative nucleolus images of mCh-CRY2-(PR)$_{13}$ at the indicated time during FRAP measurements. Scale bar, 2 μm. (**G**) Fluorescence recovery curves showing the mCh intensity over time in the photobleached region (dashed circle). FRAP measurements were performed on HeLa cells expressing mCh-CRY2-(PR)$_{13}$ after photoinduced nucleolar targeting and condensate formation. The fluorescence recovery half-time ($t_{1/2}$) was determined to be 53.8 ± 6.6 s.

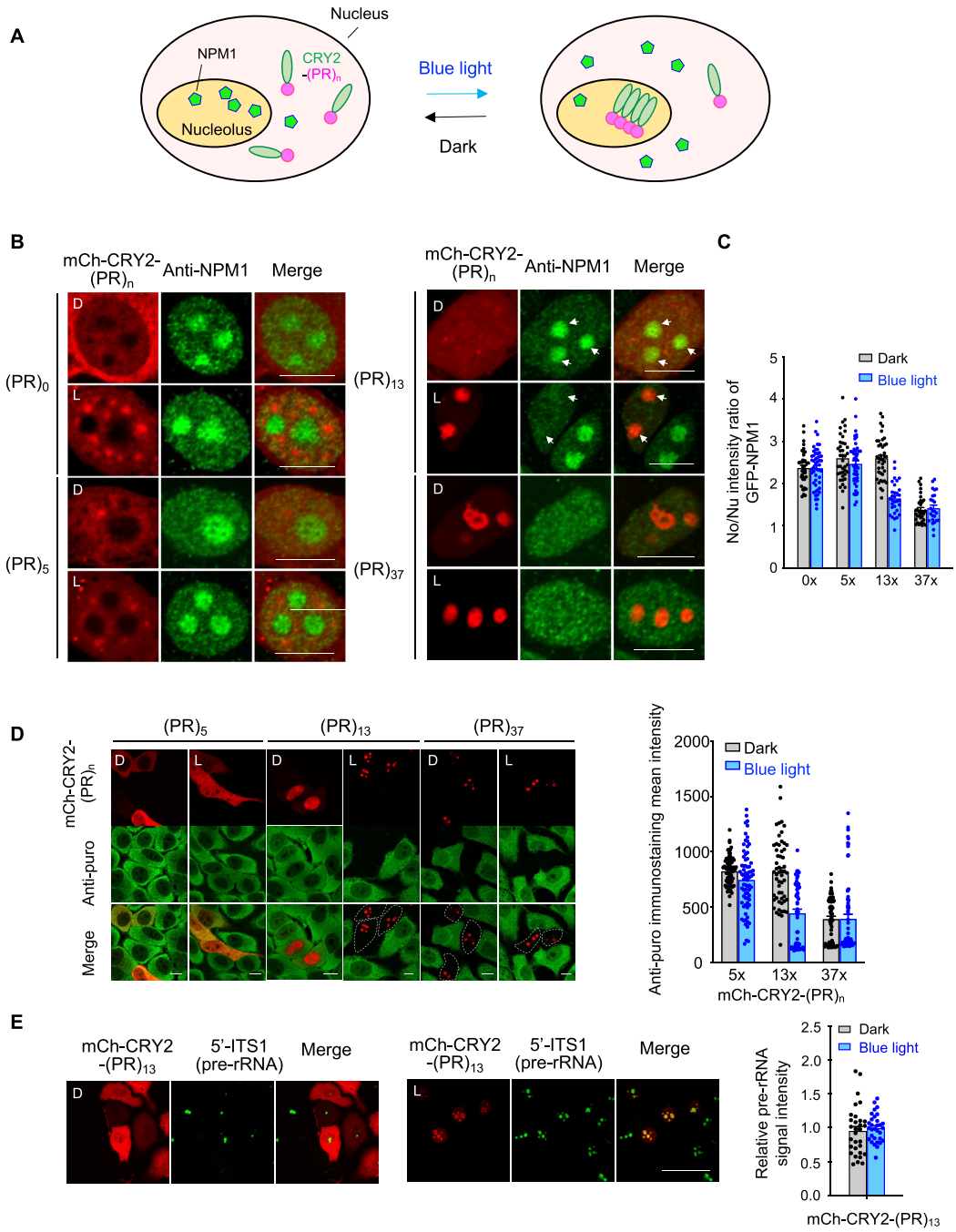

Figure 5. Light-inducible nucleolar partitioning of CRY2-$(PR)_n$ to perturb nucleolar function. (**A**) Schematic illustrating the disruption of NPM1 phase separation by nucleolus-resident mCh-CRY2-$(PR)_n$ upon blue light stimulation. (**B**) Representative confocal images of fixed HeLa cells expressing the indicated mCh-CRY2-$(PR)_n$ variants (red) after immunostaining for detecting endogenous NPM1 (green). Cells were either shielded or exposed to pulsed 470 nm light stimulation with a power density of 40 $\mu W/mm^2$ for 1 h (1-min ON + 3-min OFF cycles). A monoclonal antibody against NPM1 was used to probe endogenous nucleolar NPM1. mCh-CRY2-$(PR)_{13}$ was able to elicit the dispersion of NPM1 from the nucleoli upon photostimulation, indicating the inhibition of proper phase separation of NPM1 in a light-dependent manner. Scale bar, 10 μm. Also see Supplementary Figure S14 for larger fields of view. D, dark; L, light. (**C**) Quantification of the No/Nu ratio of the immunostaining intensity of NPM1 ($n = 33$–41 cells from three independent experiments). Cells expressing mCh-CRY2-$(PR)_{13}$ showed light-dependent dissolution of phase-separated NPM1 in the nucleolus. (**D**) Representative confocal images of HeLa cells expressing the indicated mCh-CRY2-$(PR)_n$ variants after immunostaining with an antibody against puromycin (anti-puro). Cells were either kept in the dark or exposed to pulsed light stimulation (470 nm, 40 $\mu W/mm^2$, 1 h), and then incubated with puromycin (5 μg/ml for 15 min). Newly synthesized proteins were detected by an anti-puromycin antibody. mCh-CRY2-$(PR)_{13}$ displayed a potent light-dependent suppression of nascent protein synthesis. Mean anti-puromycin immunostaining intensities were plotted on the right ($n = 56$–77 cells from three independent experiments). D, dark; L, light. Also see Supplementary Figure S15 for larger fields of view. (**E**) Visualization and quantification of pre-rRNA by FISH in HeLa cells with or without mCh-CRY2-$(PR)_n$ expression. The mean intensity of pre-rRNA staining in mCh-negative cells was set to 1, and pre-rRNA signals in mCh-CRY2-$(PR)_n$-expressing cells were then normalized. D, dark; L, blue light. Data are shown as mean ± s.e.m. ($n = 31$ cells). See Supplementary Figure S16 for more images.

filtration of CRY2-$(PR)_n$ might be able to alter the condensate formation behavior and subnuclear localization of NPM1 to cause nucleolar dysfunction. To test this idea, we examined the subnuclear localization of endogenous NPM1 with immunostaining in HeLa cells expressing mCh-CRY2-$(PR)_n$ (n = 0, 5, 13 or 37; Figure 5B). Since CRY2-$(PR)_5$ did not show light-inducible nucleolar distribution while CRY2-$(PR)_{37}$ displayed strong nucleolar accumulation regardless of photostimulation (Figure 4), they could be used as negative and positive controls, respectively, in the assay. As anticipated, cells expressing mCh-CRY2 or mCh-CRY2-$(PR)_5$ showed strong nucleolar staining for NPM1 in the absence or presence of photostimulation. In contrast, in cells expressing mCh-CRY2-$(PR)_{37}$, we observed the disappearance of nucleolar NPM1 staining regardless of light stimulation (Figure 5B and C; Supplementary Figure S14). Notably, mCh-CRY2-$(PR)_{13}$ showed photoactivatable nucleolar localization, accompanied with light-inducible suppression of NPM1 phase separation, as reflected by the disappearance of NPM1 staining in the GC region (Figure 5B and C; Supplementary Figure S14).

Given the vital importance of NPM1 in organizing ribosomal proteins and RNAs for efficient ribosome biogenesis within the nucleolus, we tested whether CRY2-$(PR)_n$ could be used to disrupt ribosome-associated function in a light-dependent manner. Since the ribosome plays a central role in protein translation, we set out to measure the efficacy of photoactivated CRY2-$(PR)_n$ in suppressing ribosome-mediated nascent protein synthesis *in situ*. To do so, we treated transfected cells with a brief pulse of puromycin, which will lead to the generation of polypeptide–puromycin conjugates and therefore enable us to detect newly synthesized polypeptides with an anti-puromycin antibody (51). In the dark, cells expressing mCh-CRY2-$(PR)_{13}$ observed strong anti-puromycin staining signals (Figure 5D, green; Supplementary Figure S15). Upon light stimulation, mCh-CRY2-$(PR)_{13}$ exhibited a predominant nucleolar distribution, accompanied with very weak or no anti-puromycin staining (Figure 5D, photoactivated mCh-CRY2-$(PR)_{13}$ in red and anti-puromycin in green; Supplementary Figure S15). It is worth noting that, in the same imaging field, cells not expressing mCh-CRY2-$(PR)_{13}$ retained strong immunostaining signals for puromycylated peptides. As negative or positive controls, we detected strong fluorescent signals in cells expressing mCh-CRY2-$(PR)_5$ but barely any signals in those transfected with mCh-CRY2-$(PR)_{37}$ (Figure 5D; Supplementary Figure S15).

Next, we examined the effect of CRY2-(PR)n on early pre-rRNA accumulation in the nucleolus by RNA FISH. A probe spanning the 18S-ITS1 junction with FAM conjugated to its 5′ end (5′ITS1) was used (Supplementary Figure S16A). Upon photostimulation, mCh-CRY2-$(PR)_n$ (n = 0–37) did not seem to alter pre-rRNA signals (Figure 5E; Supplementary Figure S16B and C). Moreover, $(PR)_{50}$ expression induces spontaneous assembly of stress granules with poor dynamics in HeLa cells followed by impaired mRNA translation, as indicated by results from a puromycin incorporation assay (52). Given the short timescale over the course of 1 h [as compared to nucleolar disruption by 4 h (16) of high concentration of actinomycin treatment (53)], we cannot exclude the possibility of an indirect effect imposed by photoactivated CRY2-$(PR)_n$, which might induce the formation of stress granules to halt protein synthesis even though no changes in cell viability were observed (Supplementary Figure S11). Together, the application of photoactivatable poly-PR repeats phenocopied the cellular effects of the C9ORF72-DPR by disrupting NPM1 nucleolar organization and suppressing ribosome-mediated protein synthesis in a light- and DPR length-dependent manner and possibly indirectly through inducing the formation of stress granules.

DISCUSSION

The nucleolus is a dynamic subnuclear compartment organized through phase separation and serves as an indispensable site for ribosome RNA synthesis, processing and ribonucleoprotein assembly for ribosome biogenesis. The engineering of a nucleolar targeting system with rapid and reversible control over nucleolar delivery of proteins of interest using optogenetic technologies (31,54,55) could advance the understanding of the biophysical principles underlying nucleolar phase separation. The control of nuclear targeting of proteins has been reported (11), but no such tools are yet available to directly control nucleolar targeting. In the current study, we utilized the NoLS comprising positively charged amino acids such as arginines and lysines that drive protein nucleolar infiltration through electrochemical interactions with negatively charged acidic nucleolar components (8). The pNUT toolkit enables customized nucleolar cargo delivery to interrogate the molecular transport dynamics within the condensates of the liquid-like nucleoli. The pNUT system is also compatible with existing tools to study the dynamic condensate composition and structure, such as the ascorbate peroxidase for nucleolar targeting and proximity labeling of nucleolar proteins and RNAs to reveal dynamic networks of protein–protein and protein–rRNA interactions (56). Of note, while CRY2 alone could partially accumulate in the PML bodies and nuclear speckle area, the CRY2-based pNUT3 could specifically deliver proteins to the GC region of the nucleolus and the Gems. Most of the LOV2-based pNUT2 deliver proteins to nucleoli, but ∼30% of pNUT2-expressing cells also showed partial pNUT2 accumulation in PML and Cajal bodies. Therefore, it is likely that pNUTs could be further improved and repurposed for inducible targeting of proteins to different nuclear bodies. It is worth mentioning that the fold change in the partitioning of pNUTs is relatively low compared to the high partitioning of natural nucleolar protein NPM1 (16) at increasing doses. The fold recruitment into nucleolus in Figure 1C was calculated as the No/Nu ratio of mCh signals. If recalculated as the nucleolar mCherry intensity ratio before and after light stimulation, LOV2-NoLS variants could reach a higher partitioning ratio upon light activation as shown in Figure 2C. In addition, given that the majority of the constructs already showed weak exclusion in the dark state (with the ratio close to 1), the fold recruitment into nucleolus or the maximum fold intensity ratio in the nucleolus is low as it was calculated as the inverse of the volume fraction. We will address this limitation in our follow-on studies.

CRY2 has been used for photoinducible oligomerization of IDRs, such as DDX4, HNRNPA1 and FUS, to

drive phase separation inside the cells (44). These optogenetic tools, however, can only modulate the concentration of molecules but lack the ability to directly control the protein delivery to a specific organellar location. In addition, a two-component optogenetic tool that uses a self-assembling ferritin core has been developed to induce IDR clustering and drive droplet condensation in the nucleoplasm but not nucleoli (15). The single-component CRY2-based pNUT3 tool described herein could be used to study the properties of the materials within the nucleoli by determining the molecular diffusion and reversibly manipulating the condensate formation of a target protein. Importantly, we have extended our engineering approach to toxic arginine-rich DPRs derived from C9ORF72, which causes neurodegenerative diseases. The CRY2-$(PR)_n$ toolkit not only enables us to characterize the nucleolar infiltration and LLPS-like condensate formation properties of pathogenic DRPs, but also allows us to perturb GC-resident NPM1 phase separation and suppress protein synthesis.

Different intrinsically disordered repeats (IDRs) or protein domains (IDPs) are critical controllers of the assembly of LLPS and nuclear bodies such as nucleoli, nuclear speckles (57), and PML and Cajal bodies (16) through concentration-dependent self-association of disordered protein regions or heterotypic interactions (16). However, the rules that govern differential partitioning of such IDRs or IDPs remain obscure. Our data suggest a differential partitioning mechanism between nuclear speckles and nucleoli governed by a local concentration (mediated by CRY2 oligomerization) and DPR length (<11 versus >11). It is worth noting that the serine/arginine domain of splicing factor 2 (SRSF2) that first localizes to the nucleolus in a hypophosphorylated state could relocalize to nuclear speckles in response to phosphorylation mediated by CDC2-like kinases 1 and 2 (CLK1/2) family kinases (58). The CRY2-$(PR)_n$ tool could provide a tool to study the mechanism governing differential partitioning and to probe the functional consequences of disordered repeats or proteins. In sum, our exciting findings support the notion of adopting optogenetic engineering approaches for probing the function of membraneless organelles and *ex vivo* modeling of neurodegeneration-associated DRP toxicity at the high spatiotemporal resolution, which can be broadly applied to interrogate other phase-separated proteins and membraneless organelles as often seen during antiviral immune response and tumorigenesis (59).

DATA AVAILABILITY

All relevant data are within the paper and its supplementary data. pNUT plasmids are available in Addgene (#175744, #175745 and #175746).

SUPPLEMENTARY DATA

Supplementary Data are available at NAR Online.

FUNDING

Welch Foundation [BE-1913-20190330 to Y.Z.]; National Institutes of Health [R01CA232017 to Y.Z., R01HL146852 and R01CA240258 to Y.H., R21GM132778 to W.L.]; Cancer Prevention and Research Institute of Texas [RP210070 to Y.Z.].

Conflict of interest statement. None declared.

REFERENCES

1. Boisvert,F.M., van Koningsbruggen,S., Navascues,J. and Lamond,A.I. (2007) The multifunctional nucleolus. *Nat. Rev. Mol. Cell Biol.*, **8**, 574–585.
2. Lafontaine,D.L.J., Riback,J.A., Bascetin,R. and Brangwynne,C.P. (2021) The nucleolus as a multiphase liquid condensate. *Nat. Rev. Mol. Cell Biol.*, **22**, 165–182.
3. Martindill,D.M. and Riley,P.R. (2008) Cell cycle switch to endocycle: the nucleolus lends a hand. *Cell Cycle*, **7**, 17–23.
4. Frottin,F., Schueder,F., Tiwary,S., Gupta,R., Korner,R., Schlichthaerle,T., Cox,J., Jungmann,R., Hartl,F.U. and Hipp,M.S. (2019) The nucleolus functions as a phase-separated protein quality control compartment. *Science*, **365**, 342–347.
5. Boulon,S., Westman,B.J., Hutten,S., Boisvert,F.M. and Lamond,A.I. (2010) The nucleolus under stress. *Mol. Cell*, **40**, 216–227.
6. Calle,A., Ugrinova,I., Epstein,A.L., Bouvet,P., Diaz,J.J. and Greco,A. (2008) Nucleolin is required for an efficient herpes simplex virus type 1 infection. *J. Virol.*, **82**, 4762–4773.
7. Stenstrom,L., Mahdessian,D., Gnann,C., Cesnik,A.J., Ouyang,W., Leonetti,M.D., Uhlen,M., Cuylen-Haering,S., Thul,P.J. and Lundberg,E. (2020) Mapping the nucleolar proteome reveals a spatiotemporal organization related to intrinsic protein disorder. *Mol. Syst. Biol.*, **16**, e9469.
8. Martin,R.M., Ter-Avetisyan,G., Herce,H.D., Ludwig,A.K., Lattig-Tunnemann,G. and Cardoso,M.C. (2015) Principles of protein targeting to the nucleolus. *Nucleus*, **6**, 314–325.
9. Musinova,Y.R., Kananykhina,E.Y., Potashnikova,D.M., Lisitsyna,O.M. and Sheval,E.V. (2015) A charge-dependent mechanism is responsible for the dynamic accumulation of proteins inside nucleoli. *Biochim. Biophys. Acta*, **1853**, 101–110.
10. Emmott,E. and Hiscox,J.A. (2009) Nucleolar targeting: the hub of the matter. *EMBO Rep.*, **10**, 231–238.
11. Niopek,D., Benzinger,D., Roensch,J., Draebing,T., Wehler,P., Eils,R. and Di Ventura,B. (2014) Engineering light-inducible nuclear localization signals for precise spatiotemporal control of protein dynamics in living cells. *Nat. Commun.*, **5**, 4404.
12. Niopek,D., Wehler,P., Roensch,J., Eils,R. and Di Ventura,B. (2016) Optogenetic control of nuclear protein export. *Nat. Commun.*, **7**, 10624.
13. He,L., Tan,P., Zhu,L., Huang,K., Nguyen,N.T., Wang,R., Guo,L., Li,L., Yang,Y., Huang,Z. *et al.* (2021) Circularly permuted LOV2 as a modular photoswitch for optogenetic engineering. *Nat. Chem. Biol.*, **17**, 915–923.
14. Tan,P., He,L., Huang,Y. and Zhou,Y. (2022) Optophysiology: illuminating cell physiology with optogenetics. *Physiol. Rev.*, https://doi.org/10.1152/physrev.00021.2021.
15. Bracha,D., Walls,M.T., Wei,M.T., Zhu,L., Kurian,M., Avalos,J.L., Toettcher,J.E. and Brangwynne,C.P. (2018) Mapping local and global liquid phase behavior in living cells using photo-oligomerizable seeds. *Cell*, **175**, 1467–1480.
16. Riback,J.A., Zhu,L., Ferrolino,M.C., Tolbert,M., Mitrea,D.M., Sanders,D.W., Wei,M.T., Kriwacki,R.W. and Brangwynne,C.P. (2020) Composition-dependent thermodynamics of intracellular phase separation. *Nature*, **581**, 209–214.
17. Jack,A., Kim,Y., Strom,A.R., Lee,D.S.W., Williams,B., Schaub,J.M., Kellogg,E.H., Finkelstein,I.J., Ferro,L.S., Yildiz,A. *et al.* (2022) Compartmentalization of telomeres through DNA-scaffolded phase separation. *Dev. Cell*, **57**, 277–290.
18. Mao,Y.S., Zhang,B. and Spector,D.L. (2011) Biogenesis and function of nuclear bodies. *Trends Genet.*, **27**, 295–306.
19. Wang,B., Zhang,L., Dai,T., Qin,Z., Lu,H., Zhang,L. and Zhou,F. (2021) Liquid–liquid phase separation in human health and diseases. *Signal Transduct. Target. Ther.*, **6**, 290.
20. Lafontaine,D.L.J., Riback,J.A., Bascetin,R. and Brangwynne,C.P. (2021) The nucleolus as a multiphase liquid condensate. *Nat. Rev. Mol. Cell Biol.*, **22**, 165–182.

21. Galganski,L., Urbanek,M.O. and Krzyzosiak,W.J. (2017) Nuclear speckles: molecular organization, biological function and role in disease. *Nucleic Acids Res.*, **45**, 10350–10368.
22. Fox,A.H., Nakagawa,S., Hirose,T. and Bond,C.S. (2018) Paraspeckles: where long noncoding RNA meets phase separation. *Trends Biochem. Sci.*, **43**, 124–135.
23. Bernardi,R. and Pandolfi,P.P. (2007) Structure, dynamics and functions of promyelocytic leukaemia nuclear bodies. *Nat. Rev. Mol. Cell Biol.*, **8**, 1006–1016.
24. Shan,X., Chiang,P.M., Price,D.L. and Wong,P.C. (2010) Altered distributions of Gemini of coiled bodies and mitochondria in motor neurons of TDP-43 transgenic mice. *Proc. Natl Acad. Sci. U.S.A.*, **107**, 16325–16330.
25. Wang,Q., Sawyer,I.A., Sung,M.H., Sturgill,D., Shevtsov,S.P., Pegoraro,G., Hakim,O., Baek,S., Hager,G.L. and Dundr,M. (2016) Cajal bodies are linked to genome conformation. *Nat. Commun.*, **7**, 10966.
26. Wu,Y.I., Frey,D., Lungu,O.I., Jaehrig,A., Schlichting,I., Kuhlman,B. and Hahn,K.M. (2009) A genetically encoded photoactivatable Rac controls the motility of living cells. *Nature*, **461**, 104–108.
27. Yao,X., Rosen,M.K. and Gardner,K.H. (2008) Estimation of the available free energy in a LOV2-J alpha photoswitch. *Nat. Chem. Biol.*, **4**, 491–497.
28. Taslimi,A., Vrana,J.D., Chen,D., Borinskaya,S., Mayer,B.J., Kennedy,M.J. and Tucker,C.L. (2014) An optimized optogenetic clustering tool for probing protein interaction and function. *Nat. Commun.*, **5**, 4925.
29. Kennedy,M.J., Hughes,R.M., Peteya,L.A., Schwartz,J.W., Ehlers,M.D. and Tucker,C.L. (2010) Rapid blue-light-mediated induction of protein interactions in living cells. *Nat. Methods*, **7**, 973–975.
30. Tao,Z., Wang,H., Xia,Q., Li,K., Li,K., Jiang,X., Xu,G., Wang,G. and Ying,Z. (2015) Nucleolar stress and impaired stress granule formation contribute to C9orf72 RAN translation-induced cytotoxicity. *Hum. Mol. Genet.*, **24**, 2426–2441.
31. He,L., Zhang,Y., Ma,G., Tan,P., Li,Z., Zang,S., Wu,X., Jing,J., Fang,S., Zhou,L. *et al.* (2015) Near-infrared photoactivatable control of Ca^{2+} signaling and optogenetic immunomodulation. *eLife*, **4**, e10024.
32. Ma,G., Wen,S., He,L., Huang,Y., Wang,Y. and Zhou,Y. (2017) Optogenetic toolkit for precise control of calcium signaling. *Cell Calcium*, **64**, 36–46.
33. Shin,Y., Chang,Y.C., Lee,D.S.W., Berry,J., Sanders,D.W., Ronceray,P., Wingreen,N.S., Haataja,M. and Brangwynne,C.P. (2018) Liquid nuclear condensates mechanically sense and restructure the genome. *Cell*, **175**, 1481–1491.
34. O'Donohue,M.F., Choesmel,V., Faubladier,M., Fichant,G. and Gleizes,P.E. (2010) Functional dichotomy of ribosomal proteins during the synthesis of mammalian 40S ribosomal subunits. *J. Cell Biol.*, **190**, 853–866.
35. Fueller,J., Herbst,K., Meurer,M., Gubicza,K., Kurtulmus,B., Knopf,J.D., Kirrmaier,D., Buchmuller,B.C., Pereira,G., Lemberg,M.K. *et al.* (2020) CRISPR–Cas12a-assisted PCR tagging of mammalian genes. *J. Cell Biol.*, **219**, e201910210.
36. Scott,M.S., Boisvert,F.M., McDowall,M.D., Lamond,A.I. and Barton,G.J. (2010) Characterization and prediction of protein nucleolar localization sequences. *Nucleic Acids Res.*, **38**, 7388–7399.
37. Scott,M.S., Troshin,P.V. and Barton,G.J. (2011) NoD: a nucleolar localization sequence detector for eukaryotic and viral proteins. *BMC Bioinformatics*, **12**, 317.
38. Peisley,A., Wu,B., Xu,H., Chen,Z.J. and Hur,S. (2014) Structural basis for ubiquitin-mediated antiviral signal activation by RIG-I. *Nature*, **509**, 110–114.
39. Zhang,C., Shang,G., Gui,X., Zhang,X., Bai,X.C. and Chen,Z.J. (2019) Structural basis of STING binding with and phosphorylation by TBK1. *Nature*, **567**, 394–398.
40. Alberti,S. (2017) Phase separation in biology. *Curr. Biol.*, **27**, R1097–R1102.
41. Bugaj,L.J., Choksi,A.T., Mesuda,C.K., Kane,R.S. and Schaffer,D.V. (2013) Optogenetic protein clustering and signaling activation in mammalian cells. *Nat. Methods*, **10**, 249–252.
42. Feric,M., Vaidya,N., Harmon,T.S., Mitrea,D.M., Zhu,L., Richardson,T.M., Kriwacki,R.W., Pappu,R.V. and Brangwynne,C.P. (2016) Coexisting liquid phases underlie nucleolar subcompartments. *Cell*, **165**, 1686–1697.
43. Park,H., Kim,N.Y., Lee,S., Kim,N., Kim,J. and Heo,W.D. (2017) Optogenetic protein clustering through fluorescent protein tagging and extension of CRY2. *Nat. Commun.*, **8**, 30.
44. Shin,Y., Berry,J., Pannucci,N., Haataja,M.P., Toettcher,J.E. and Brangwynne,C.P. (2017) Spatiotemporal control of intracellular phase transitions using light-activated optoDroplets. *Cell*, **168**, 159–171.
45. Boeynaems,S., Bogaert,E., Kovacs,D., Konijnenberg,A., Timmerman,E., Volkov,A., Guharoy,M., De Decker,M., Jaspers,T., Ryan,V.H. *et al.* (2017) Phase separation of C9orf72 dipeptide repeats perturbs stress granule dynamics. *Mol. Cell*, **65**, 1044–1055.
46. Loveland,A.B., Svidritskiy,E., Susorov,D., Lee,S., Park,A., Demo,G., Gao,F.-B. and Korostelev,A.A. (2020) Ribosome inhibition by C9ORF72-ALS/FTD-associated poly-PR and poly-GR proteins revealed by cryo-EM. bioRxiv doi: https://doi.org/10.1101/2020.08.30.274597, 31 August 2020, preprint: not peer reviewed.
47. White,M.R., Mitrea,D.M., Zhang,P., Stanley,C.B., Cassidy,D.E., Nourse,A., Phillips,A.H., Tolbert,M., Taylor,J.P. and Kriwacki,R.W. (2019) C9orf72 poly(PR) dipeptide repeats disturb biomolecular phase separation and disrupt nucleolar function. *Mol. Cell*, **74**, 713–728.
48. Taylor,N.O., Wei,M.T., Stone,H.A. and Brangwynne,C.P. (2019) Quantifying dynamics in phase-separated condensates using fluorescence recovery after photobleaching. *Biophys. J.*, **117**, 1285–1300.
49. McSwiggen,D.T., Mir,M., Darzacq,X. and Tjian,R. (2019) Evaluating phase separation in live cells: diagnosis, caveats, and functional consequences. *Genes Dev.*, **33**, 1619–1634.
50. Mitrea,D.M., Cika,J.A., Guy,C.S., Ban,D., Banerjee,P.R., Stanley,C.B., Nourse,A., Deniz,A.A. and Kriwacki,R.W. (2016) Nucleophosmin integrates within the nucleolus via multi-modal interactions with proteins displaying R-rich linear motifs and rRNA. *eLife*, **5**, e13571.
51. Schmidt,E.K., Clavarino,G., Ceppi,M. and Pierre,P. (2009) SUnSET, a nonradioactive method to monitor protein synthesis. *Nat. Methods*, **6**, 275–277.
52. Lee,K.H., Zhang,P., Kim,H.J., Mitrea,D.M., Sarkar,M., Freibaum,B.D., Cika,J., Coughlin,M., Messing,J., Molliex,A. *et al.* (2016) C9orf72 dipeptide repeats impair the assembly, dynamics, and function of membrane-less organelles. *Cell*, **167**, 774–788.
53. Reich,E., Franklin,R.M., Shatkin,A.J. and Tatum,E.L. (1962) Action of actinomycin D on animal cells and viruses. *Proc. Natl Acad. Sci. U.S.A.*, **48**, 1238–1245.
54. Tan,P., He,L., Han,G. and Zhou,Y. (2017) Optogenetic immunomodulation: shedding light on antitumor immunity. *Trends Biotechnol.*, **35**, 215–226.
55. Ma,G., He,L., Liu,S., Xie,J., Huang,Z., Jing,J., Lee,Y.T., Wang,R., Luo,H., Han,W. *et al.* (2020) Optogenetic engineering to probe the molecular choreography of STIM1-mediated cell signaling. *Nat. Commun.*, **11**, 1039.
56. Fazal,F.M., Han,S., Parker,K.R., Kaewsapsak,P., Xu,J., Boettiger,A.N., Chang,H.Y. and Ting,A.Y. (2019) Atlas of subcellular RNA localization revealed by APEX-seq. *Cell*, **178**, 473–490.
57. Greig,J.A., Nguyen,T.A., Lee,M., Holehouse,A.S., Posey,A.E., Pappu,R.V. and Jedd,G. (2020) Arginine-enriched mixed-charge domains provide cohesion for nuclear speckle condensation. *Mol. Cell*, **77**, 1237–1250.
58. Kwon,I., Xiang,S., Kato,M., Wu,L., Theodoropoulos,P., Wang,T., Kim,J., Yun,J., Xie,Y. and McKnight,S.L. (2014) Poly-dipeptides encoded by the C9orf72 repeats bind nucleoli, impede RNA biogenesis, and kill cells. *Science*, **345**, 1139–1145.
59. Alberti,S. and Dormann,D. (2019) Liquid–liquid phase separation in disease. *Annu. Rev. Genet.*, **53**, 171–194.